Comprehensive Report

Carbon dioxide fixation, Electrochemistry, Bismuth, Formic acid, Selectivity

CJC Chinese Journal of Chemistry 中国化学 · An International Journal

Structural Optimization of Metal Oxyhalide for CO_2 Reduction with High Selectivity and Current Density

Fan-Lu Meng,[‡,a,b] Qi Zhang,[‡,a,c] Yan-Xin Duan,[‡,b] Kai-Hua Liu,[a,b] and Xin-Bo Zhang*[,a]

[a] *State Key Laboratory of Rare Earth Resource Utilization, Changchun Institute of Applied Chemistry, Chinese Academy of Sciences, Changchun, Jilin 130022, China*
[b] *Key Laboratory of Automobile Materials, Ministry of Education and College of Materials Science and Engineering, Jilin University, Changchun, Jilin 130012, Jilin, China*
[c] *Hunan Key Laboratory for Micro-Nano Energy Materials and Device, Department of Physics, Xiangtan University, Xiangtan, Hunan 411105, China*

Cite this paper: *Chin. J. Chem.* **2020**, *38*, 1752—1756. **DOI: 10.1002/cjoc.202000203**

Summary of main observation and conclusion Electrochemical CO_2 reduction into value-added liquid fuels using CO_2 neutral renewable energy sources is very promising to solve climatic issues. In order to realize their practical applications, highly active and inexpensive electrocatalysts are urgently required. In this study, we have experimentally achieved high electrocatalytic activity towards CO_2 reduction for the synthesis of formate with an enhanced current density of 15.1 mA·cm^{-2} and significantly improved Faradaic efficiency of 98.4% upon electrochemical reduced ultrathin bismuth oxybromide nanosheets. Moreover, the stable performance during 24 h of operation is also obtained. Furthermore, by detecting the exposed crystal plane after surface reorganization and applying density functional theory calculations, the possible reaction pathways and catalytic active plane of the derived bismuth catalyst are put forward, which would offer basic and design principles to directly develop the optimized metal Bi catalysts for enhanced electrocatalytic CO_2 conversion to formate.

Background and Originality Content

The consumption of non-renewable fossil fuels is accelerating rapidly, which brings about excessive emissions of greenhouse gas CO_2, destroying the balance of natural carbon cycles, and leading to worsening global climate change.[1-4] Electrochemical CO_2 reduction into value-added chemical compounds like hydrocarbon fuels,[5-9] or carbon monoxide (for syngas)[10-13] will be a promising solution, especially actuated by wind and solar energy as CO_2 neutral sustainable sources. Despite excellent prospects, two critical bottlenecks imped its commercial application available greatly, including broad product distribution on hydrocarbon producing due to numerous possible reaction pathways, and low energy efficiency due to the high overpotential.[14-16] To address these issues, lots of metals-based materials have been investigated to catalyze electrochemical reduction of CO_2 into a series of products over past years.

Among various products, a few have achieved high yield, and formate is the particular one as a high value-added chemical. bismuth (Bi) is a newly discovered attractive catalyst for CO_2 conversion towards the synthesis of formate in aqueous electrolyte due to its non-toxic and cheap feature.[17-20] However, the reported activities suffer from either low Faradaic efficiencies or low catalytic current densities or deactivation in continuous electrolysis, in spite of their special nanostructures. For better performance, it is crucial to develop a more efficient strategy. Recently, oxide-derived metal nanostructures are regard as valid solution to enable CO_2 reduction with high selectivity at low overpotential,[21-25] of which, active sites of derived zero-valent metals are mostly in-situ created by surface atom reorganization along with the electrochemical reduction process. Unique designed structures to facilitate this process are always effective. Two-dimensional (2D) ultrathin nanostructure seems to be an attractive option, on account of a ultralarge specific surface area, rapid interfacial charge transfers between the reagents and electrode, and low-coordinated steps, edges, and kinks.[26-32] In this case, more interior atoms are expected exposed in reduction process to ensure a great number of surface active sites.

Following up, bismuth oxybromide (BiOBr) with a typical feature of $[Bi_2O_2]$ layer interleaved by double layers of halogen atoms tends forming nanosheet-like structure, and morphology preservation during the structural transformation,[33] which should be an effective candidate. With this in mind, herein, as a proof-of-concept experiment, we have developed ideal 2D BiOBr ultrathin nanosheets (Bi-NSS) realizing high activity for CO_2 electrochemical reduction with an enhanced partial current density and significantly improved Faradaic efficiency of 98.4% for formate and long-term stability (24 h). In addition, based on the detected exposed crystal surface of derived Bi catalysts after reorganization under electrochemical reduction, we applied density functional theory (DFT) calculations for theoretical studies to explore the origin. Possible reaction pathways and catalytic active plane are put forward accordingly, which would offer basic and design principles to directly prepare the optimized metal Bi catalysts.

Results and Discussion

The Bi-NSS was synthesized with a simple solvothermal method by adjusting reactants. In which, the use of 1-hexadecyl-3-methylimidazolium bromide (C16MIMBr) and additional water is proved crucial for enforcing an ultrathin sheet-like morphology. The employed scanning electron microscopy (SEM) and transmission electron microscopy (TEM) present the well-defined 2D ultrathin nanostructure (Figures 1a and b). A thickness of ~7.01 nm is confirmed by atomic force microscopy (AFM) images in Figure 1c. All diffraction peaks in X-ray diffraction (XRD) pattern can be well indexed to the BiOBr phase (PDF-# 09-0393) (Figure S1a). Figure 1d displays the high-resolution TEM (HRTEM) image of as-prepared Bi-NSS, the lattice fringe of the layer distance is 0.278 nm, corresponding to the lattice plane of (110) of BiOBr. The selected-area electron diffraction (SAED) further reveals the

*E-mail: xbzhang@ciac.ac.cn
‡ These authors contributed equally to this work.

For submission: https://mc.manuscriptcentral.com/cjoc
For articles: https://onlinelibrary.wiley.com/journal/16147065

high purity and single crystalline nature of BI-NSS (Figure 1e). The uniform ingredient is observed by energy-dispersive X-ray element mapping (Figure 1f). This 2D ultrathin nanostructure usually brings a ultralarge specific surface area, which is confirmed by the nitrogen (N_2) absorption-desorption isotherms (Figure S2a). The Brunauer-Emmett-Teller (BET) surface area is determined to be 59.8 $m^2 \cdot g^{-1}$.

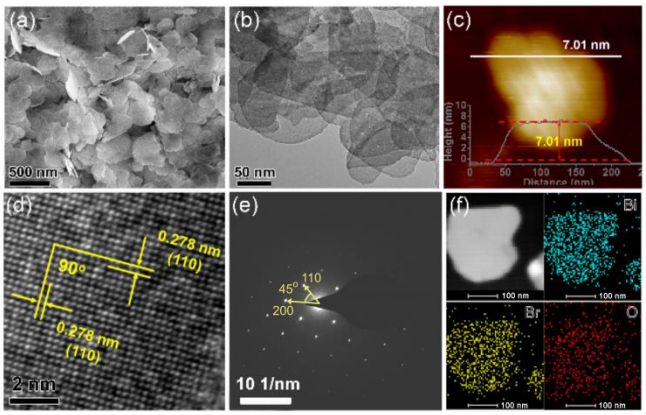

Figure 1 (a) SEM, (b) TEM, and (c) AFM image of Bi-NSS. (d) The corresponding high-magnification TEM (HRTEM) image. (e) The SAED image. (f) HADDF image and the corresponding element mapping of Bi-NSS.

For comparison, by adjusting reactants, experimental verifications are then performed under the same initial conditions and controlling temperature to synthesize samples with morphology variation to investigate the advantages of ultrathin 2D structure of Bi-NSS. Detailedly, without additional water in ethylene glycol solvent, the ultrathin nanosheet disappears, the sample with a 3D flower morphology assembled by lamellar structure is produced (Figure S3), which is named as BiOBr flowers (Bi-FS). In sharp contrast, once replacing the surfactant with inorganic KBr as Br resource, the sample with enlarged sphere morphology called after BiOBr spheres (Bi-SS) turns out, same characterizations confirm its morphology, phase and elements (Figure S4). Based on the above structure analysis, both should own much decreased specific surface area compared to Bi-NSS, which are confirmed to be 24.3 and 9.8 $m^2 \cdot g^{-1}$, respectively (Figure S2a). X-ray photoelectron spectroscopy (XPS) is then performed to analyze surface compositions (Figures S1b—d), wherein, different chemical states of Bi 4f and Br 3d between them appear, which should be attributed to low-coordination of the ultrathin 2D structure of Bi-NSS. As a contrast sample, the chemical reduced metal Bi from BiOBr by $NaBH_4$ is also prepared and characterized named as CR-Bi (Figure S5), proving its pure Bi metal phase with a granule morphology.

The performance of electrocatalytic CO_2 reduction for samples is characterized in a CO_2-saturated 0.1 M $KHCO_3$ solution by casting samples on a glass carbon electrode, using a H-type three-electrode set-up separated by Nafion (112) membrane. Before activity test, the samples of BiOBr were activated by applying a cathodic current of –5.0 $mA \cdot cm^{-2}$ on working electrodes until reaching a stable potential without change (Figure S6). Linear sweep voltammetry (LSV) is carried out firstly. Obviously, the cathodic current is enhanced greatly in the presence of CO_2 compared to Ar-saturated solution (Figure 2a), which provides a direct evidence for the electrocatalytic activity towards CO_2 reduction. The reduction current density complies with the following order: Bi-NSS > Bi-FS > Bi-SS > CR-Bi, preliminarily illustrating a higher activity of Bi-NSS and the advanced oxide strategy. In order to further evaluate the selectivity, chronoamperometric measurements at each potential are performed for 2 h to collect the liquid products (Figure S7), which are quantified by nuclear magnetic resonance (^{1}H NMR) analysis. The gas products are quantified by gas chromatography (GC) using potential gradient tests, in which, only formate, CO, and H_2 without multi-carbon products are identified after the electrochemical process stopping (Figure S8). Figure 2b shows the faradaic efficiency (FE) for formate product as a function of potentials. Wherein, the Bi-NSS electrode reaches a maximum FE of 98.4% at a cathodic potential of –1.2 V versus RHE and a broad plateau of high formate yields is also observed between –0.9 and –1.3 V (a very high selectivity from 78.9% to 98.4%). Remarkably, the high FE of 98.4% towards formate is among the highest reported results (Table S1). In contrast, the highest FE of Bi-FS and Bi-SS are 93.3% and 85.6%, respectively, slightly lower than that of Bi-NSS. In addition, the potential range with a selectivity higher than 70% for them becomes narrow. Compared to these BiOBr derived samples, the CR-Bi shows much lower FE of 75.9%, proving this efficient oxide-derived strategy. Notably, in the whole potential range, formate is always the major CO_2 reduction product except the competition of hydrogen evolution reaction, whether it is BiOBr derived Bi samples or CR-Bi (Figure S9), meaning their superior single conversion or product selectivity.

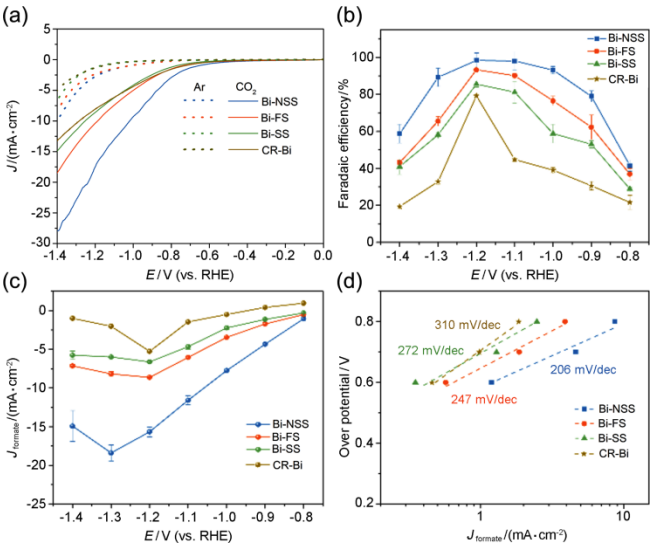

Figure 2 Data of electroreduction of CO_2 to formate shown for Bi-NSS, Bi-FS, Bi-SS, and CR-Bi. (a) Linear sweep voltammetric curves in a CO_2-saturated (solid line) and Ar-saturated (dashed line) 0.1 M $KHCO_3$ aqueous solution. (b) Faradaic efficiencies of formate at each given potential. (c) Partial current densities toward formate at each given potential. (d) Tafel plots.

Taking into account its incorporation of both the reaction rate and selectivity, the partial current density of formate formation ($J_{formate}$) should be a very comprehensive metric, which is shown in Figure 2c. The $J_{formate}$ of Bi-NSS realizes the peak value as high as –18.4 $mA \cdot cm^{-2}$ at –1.3 V. Moreover, Bi-NSS attains a maximum turnover frequency (TOF) at –1.3 V (Figure S10). In sharp contrast, the highest current density for Bi-FS, Bi-SS and CR-Bi are 8.6, 6.6 and 6.3 $mA \cdot cm^{-2}$, respectively. But beyond that, both are reached at –1.2 V, meaning higher overpotential couldn't ensure higher product, representing different kinetic rates. Figure 2d reveals that Tafel slope of Bi-NSS is approximately 206 mV/decade, which is much smaller than that of Bi-FS (247 mV/decade), Bi-SS (272 mV/decade), and CR-Bi (310 mV/decade), indicating higher CO_2 reduction kinetics. Energy conversion efficiency is another key parameter in benchmarking electrocatalysts. The energy efficiency of the formation of formate is then evaluated according to early report, which is shown in Figure 3a.[22,34] The low overpotential together with a high FE of Bi-NSS contributes to an higher energy

efficiency. The stability of catalysts is very crucial involving practical applications. Hence, the long-term durability of Bi-NSS is evaluated in a chronoamperometric experiment at an applied potential of –1.2 V for 24 h. The product distribution with respect to time is examined; the relative FE of formate is then measured and calculated at intervals. As shown in Figure 3b, notably, the Bi-NSS catalyst exhibits a very stable total geometric current density during 24 h of continuous electrolysis. In the end, the FE of formate for Bi-NSS is approximately 95.0% with a decline of only about 3.4%. Such high activity, selectivity, and stability consequently distinguish Bi-NSS as a prospective means for CO_2 reduction.

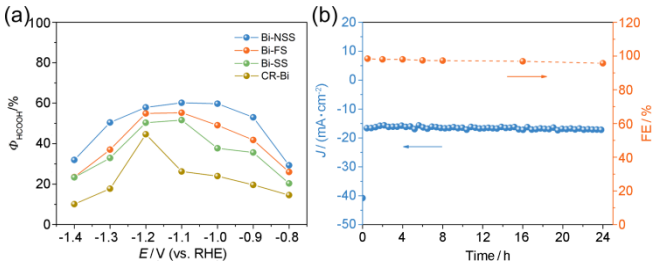

Figure 3 (a) The cathodic energy efficiency ($\Phi_{formate}$) for Bi-NSS, Bi-FS, Bi-SS, and CR-Bi at different applied potentials. (b) Chronoamperometry results at the corresponding potentials with the highest Faradaic efficiencies of –1.2 V versus RHE and the corresponding FE results at a series of potentials.

The morphologic structure, chemical composition, and phase structure of derived Bi samples after continuous electrolysis are characterized to analyze catalytic centers to explain this superior activity. XRD patterns firstly confirm the metallic Bi (PDF#44-1246) for Bi-NSS, Bi-FS, and Bi-SS without other phases (Figure S11a). Besides, the high-index (012), (110) and (104) planes are preferentially developed on these samples. The HRTEM image shows the resolved lattice fringes of Bi (110) plane with a spacing of 0.227 nm for reduced Bi-NSS (Figure S12d). Lattice fringes of Bi (012) plane with a spacing of 0.328 nm for Bi-FS (Figure S13d inset) and (104) plane with 0.237 nm for Bi-SS (Figure S14d inset) are observed, respectively. Both SEM and TEM images reflect that, Bi-NSS reserves good sheet-like morphology after the 24 h continuous reaction (Figure S12a-c). Bi-FS and Bi-SS also display well morphologic structure stability (Figures S13a—c and S14a—c). However, all samples become much rough compared to their original state, interconnected nanoparticles arise. Higher specific surface area with low-coordination of ultrathin nanosheet should render more exposed interior atoms after surface reorganization leading to enlarged active sites for Bi-NSS, which can be assessed by electrochemical active surface area (ECSA). An about double ECSA for Bi-NSS is realized than Bi-FS, the ECSA of Bi-FS is about a quarter higher than that of Bi-SS and CR-Bi (Figures S15 and S16). The XPS spectra shown in Figures S11b—d prove more effective reduction to CO_2 by active metallic Bi with the advantage of untralthin sheet structure. The electrochemical impedance spectroscopy (EIS) technique is then used to provide deep insight into the kinetics during CO_2 reduction process. A lowest charge-transfer resistance is observed for Bi-NSS, associated with its superior CO_2 reduction activity (Figure S17). Experimentally, all above reduced BiOBr samples exhibit excellent CO_2 reduction selectivity for formate, however, the origin is still unknown.

To gain a deeper understanding on the origin of the possible reaction mechanism and pathways for this high selectivity of CO_2 conversion to formate, the first-principle calculations based on the DFT were carried out to lift some veils, including the undefined active facet, the optimal reaction route, and the rate-determining step during the reaction, in which, the Gibbs free energy (ΔG) is adopted as a descriptor to estimate the catalytic activity. According to the ΔG calculations results shown in Figure 4, it is found that all Bi (110), Bi (012) and Bi (104) planes observed in three samples have fine and similar performance for the reduction into formate following the HCOO* reaction mechanism (Equations S6a—8b), respectively. Besides, the first hydrogenation process to form HCOO* has higher energy barrier compared with other element reaction, indicating that it is the rate-determining step. The reaction barrier of the rate-determining step for all the derived Bi catalysts is around 0.7 eV, which is almost consistent with the experimentally measured onset potential. It is noteworthy that, compared to Bi (104) and Bi (012), the Bi (110) can possess higher catalytic performance due to its lower reaction barrier of 0.67 eV. Moreover, the reaction barriers for the reduction of CO_2 into CO and HER competitive reaction are both obviously higher than that of the formation of formate (Figures S18 and S19), further implying the high selectivity for formate product.

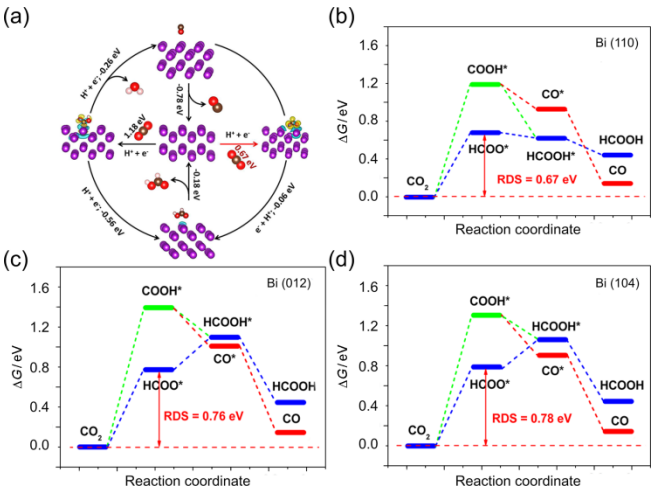

Figure 4 DFT calculation results on the CO_2-to-formate reduction reaction pathways for various possible Bi planes. (a) Reaction mechanism schematic diagram for CO_2 reduction reaction in Bi (110), including the reaction barrier of each element reaction and the charge density difference images of the intermediate state (the yellow and cyan iso-surface represent the electron accumulation and the electron depletion, respectively. The corresponding Gibbs free energy diagram (the RDS refers to the rate-determining step) on (b) Bi (110), (c) Bi (012), and (d) Bi (104).

Conclusions

In summary, we have developed an ideal BiOBr ultrathin 2D nanosheet to enhance the activity of Bi in CO_2 reduction. The electrochemical measurements indicate high catalytic activity and selectivity of electrochemical reduced BiOBr ultrathin 2D nanosheet catalyst towards conversion of CO_2 to formate with an enhanced current density of 15.1 mA·cm^{-2} and significantly improved Faradaic efficiency of 98.4% upon electrochemical reduced ultrathin BiOBr nanosheets. Furthermore, the stable performance during 24 h of operation is also obtained. The comparative materials produced by adjusting reactants and the chemical reduced sample display worse activity, which identifies tremendous advantages based on ultrathin 2D structure and oxide derived strategy. Furthermore, by detecting the exposed crystal plane after surface reorganization and applying theory calculations, the possible reaction pathways and catalytic active plane of the derived Bi catalyst are put forward, which would offer basic and design principles to directly develop the optimized metal Bi catalysts for enhanced electrocatalytic CO_2 conversion to formate.

Supporting Information

The supporting information for this article is available on the WWW under https://doi.org/10.1002/cjoc.202000203.

Acknowledgement

This work was financially supported by the Strategic Priority Research Program of the Chinese Academy of Sciences (XDA21010210), the National Key R&D Program of China (2016YFB0100103), the National Natural Science Foundation of China (21725103 and 21905269), the Jilin Province Science and Technology Development Plan Funding Project (20180101203JC, 20200201079JC), the National & Local United Engineering Lab for Power Battery and Jilin Province Key Laboratory of Low Carbon Chemical Power Sources.

References

[1] Wang, Z. L.; Li, C.; Yamauchi, Y. Nanostructured nonprecious metal catalysts for electrochemical reduction of carbon dioxide. *Nano Today* **2016**, *11*, 373–391.

[2] Feng, J.; Zeng, S.; Feng, J.; Dong, H.; Zhang, X. CO_2 electroreduction in ionic liquids: a review. *Chin. J. Chem.* **2018**, *36*, 961–970.

[3] Zhang, Z.; Ahmad, F.; Zhao, W.; Yan, W.; Zhang, W.; Huang, H.; Ma, C.; Zeng, J. Enhanced electrocatalytic reduction of CO_2 via chemical coupling between indium oxide and reduced graphene oxide. *Nano Lett.* **2019**, *19,* 4029–4034.

[4] Jia, L.; Yang, H.; Deng, J.; Chen, J.; Zhou, Y.; Ding, P.; Li, L.; Han, N.; Li, Y. Copper-Bismuth Bimetallic Microspheres for Selective Electrocatalytic Reduction of CO_2 to Formate. *Chin. J. Chem.* **2019**, *37*, 497–500.

[5] Gao, S.; Gu, B.; Jiao, X.; Sun, Y.; Zu, X.; Yang, F.; Xie, Y. Highly efficient and exceptionally durable CO_2 photoreduction to methanol over freestanding defective single-unit-cell bismuth vanadate layers. *J. Am. Chem. Soc.* **2017**, *139*, 3438–3445.

[6] Gao, S.; Lin, Y.; Jiao, X.; Sun, Y.; Luo, Q.; Zhang, W.; Xie, Y. Partially oxidized atomic cobalt layers for carbon dioxide electroreduction to liquid fuel. *Nature* **2016**, *529*, 68–71.

[7] He, J.; Dettelbach, K. E.; Salvatore, D. A.; Li, T.; Berlinguette, C. P. High-Throughput Synthesis of Mixed-Metal Electrocatalysts for CO_2 Reduction. *Angew. Chem. Int. Ed.* **2017**, *56*, 6068–6072.

[8] Li, Y. C.; Wang, Z.; Yuan, T.; Nam, D. H.; Luo, M.; Wicks, J.; Chen, B.; Li, J.; Li, F.; de Arquer, F. P. G.; Wang, Y. Binding site diversity promotes CO_2 electroreduction to ethanol. *J. Am. Chem. Soc.* **2019**, *141*, 8584–8591.

[9] Zheng, W.; Yang, J.; Chen, H.; Hou, Y.; Wang, Q.; Gu, M.; He, F.; Xia, Y.; Xia, Z.; Li, Z.; Yang, B. Atomically Defined Undercoordinated Active Sites for Highly Efficient CO_2 Electroreduction. *Adv. Funct. Mater*. **2020**, *30*, 1907658.

[10] Gu, J.; Hsu, C. S.; Bai, L.; Chen, H. M.; Hu, X. Atomically dispersed Fe^{3+} sites catalyze efficient CO_2 electroreduction to CO. *Science* **2019**, *364*, 1091–1094.

[11] Yang, H.; Hu, Y. W.; Chen, J. J.; Balogun, M. S.; Fang, P. P.; Zhang, S.; Chen, J.; Tong, Y. Intermediates Adsorption Engineering of CO_2 Electroreduction Reaction in Highly Selective Heterostructure Cu-Based Electrocatalysts for CO Production. *Adv. Energy Mater.* **2019**, *9*, 1901396.

[12] Yang, H.; Hu, Y. W.; Chen, J. J.; Balogun, M. S.; Fang, P. P.; Zhang, S.; Chen, J.; Tong, Y. CO_2 Electroreduction: Intermediates Adsorption Engineering of CO_2 Electroreduction Reaction in Highly Selective Heterostructure Cu-Based Electrocatalysts for CO Production. *Adv. Energy Mater.* **2019**, *9*, 1970107.

[13] Karapinar, D.; Huan, N. T.; Ranjbar Sahraie, N.; Li, J.; Wakerley, D.; Touati, N.; Zanna, S.; Taverna, D.; Galvão Tizei, L. H.; Zitolo, A.; Jaouen, F. Electroreduction of CO_2 on Single-Site Copper-Nitrogen-Doped Carbon Material: Selective Formation of Ethanol and Reversible Restructuration of the Metal Sites. *Angew. Chem. Int. Ed.* **2019**, *58*, 15098–15103.

[14] Shi, L.; Zhang, Y.; Han, X.; Niu, D.; Sun, J.; Yang, J. Y.; Hu, S.; Zhang, X. SDS-modified Nanoporous Silver as an Efficient Electrocatalyst for Selectively Converting CO_2 to CO in Aqueous Solution. *Chin. J. Chem.* **2019**, *37*, 337–341.

[15] Zhu, D. D.; Liu, J. L.; Qiao, S. Z. Recent advances in inorganic heterogeneous electrocatalysts for reduction of carbon dioxide. *Adv. Mater.* **2016**, *28*, 3423–3452.

[16] Dunwell, M.; Lu, Q.; Heyes, J. M.; Rosen, J.; Chen, J. G.; Yan, Y.; Jiao, F.; Xu, B. The central role of bicarbonate in the electrochemical reduction of carbon dioxide on gold. *J. Am. Chem. Soc.* **2017**, *139*, 3774–3783.

[17] Liu, S.; Lu, X. F.; Xiao, J.; Wang, X.; Lou, X. W. Bi_2O_3 Nanosheets Grown on Multi-Channel Carbon Matrix to Catalyze Efficient CO_2 Electroreduction to HCOOH. *Angew. Chem. Int. Ed.* **2019**, *58*, 13828–13833.

[18] Lv, W.; Zhou, J.; Bei, J.; Zhang, R.; Wang, L.; Xu, Q.; Wang, W. Electrodeposition of nano-sized bismuth on copper foil as electrocatalyst for reduction of CO_2 to formate. *Appl. Surf. Sci.* **2017**, *393*, 191–196.

[19] Koh, J. H.; Won, D. H.; Eom, T.; Kim, N. K.; Jung, K. D.; Kim, H.; Hwang, Y. J.; Min, B. K. Facile CO_2 electro-reduction to formate via oxygen bidentate intermediate stabilized by high-index planes of Bi dendrite catalyst. *ACS Catal.* **2017**, *7*, 5071–5077.

[20] Kim, S.; Dong, W. J.; Gim, S.; Sohn, W.; Park, J. Y.; Yoo, C. J.; Jang, H. W.; Lee, J. L. Shape-controlled bismuth nanoflakes as highly selective catalysts for electrochemical carbon dioxide reduction to formate. *Nano Energy* **2017**, *39*, 44–52.

[21] Chen, S.; Su, Y. Q.; Deng, P.; Qi, R.; Zhu, J.; Chen, J.; Wang, Z.; Zhou, L.; Guo, X. P.; Xia, B. Y. Highly Selective Carbon Dioxide Electroreduction on Structure-evolved Copper Perovskite Oxide toward Methane Production. *ACS Catal.* **2020**, *10*, 4640–4646.

[22] Fu, Y.; Wang, T.; Zheng, W.; Lei, C.; Yang, B.; Chen, J.; Li, Z.; Lei, L.; Yuan, C.; Hou, Y. Nanoconfined tin oxide within N-doped nanocarbon supported on electrochemically exfoliated graphene for efficient electroreduction of CO_2 to formate and C1 products. *ACS Appl. Mater. Interfaces* **2020**, *12,* 16178–16185.

[23] Lei, Q.; Zhu, H.; Song, K.; Wei, N.; Liu, L.; Zhang, D.; Yin, J.; Dong, X.; Yao, K.; Wang, N.; Li, X. Investigating the Origin of Enhanced C2+ Selectivity in Oxide-/Hydroxide-derived Copper Electrodes during CO_2 Electroreduction. *J. Am. Chem. Soc.* **2020**, *142*, 4213–4222.

[24] Choi, Y. W.; Scholten, F.; Sinev, I.; Roldan Cuenya, B. Enhanced Stability and CO/Formate Selectivity of Plasma-Treated SnO_x/AgO_x Catalysts during CO_2 Electroreduction. *J. Am. Chem. Soc.* **2019**, *141*, 5261–5266.

[25] Kumar, B.; Atla, V.; Brian, J. P.; Kumari, S.; Nguyen, T. Q.; Sunkara, M.; Spurgeon, J. M. Reduced SnO_2 porous nanowires with a high density of grain boundaries as catalysts for efficient electrochemical CO_2-into-HCOOH conversion. *Angew. Chem. Int. Ed.* **2017**, *56*, 3645–3649.

[26] Zhao, Y.; Zhang, J.; Wu, W.; Guo, X.; Xiong, P.; Liu, H.; Wang, G. Cobalt-doped MnO_2 ultrathin nanosheets with abundant oxygen vacancies supported on functionalized carbon nanofibers for efficient oxygen evolution. *Nano Energy* **2018**, *54*, 129–137.

[27] Zhao, Y.; Jia, X.; Chen, G.; Shang, L.; Waterhouse, G. I.; Wu, L. Z.; Tung, C. H.; O'Hare, D.; Zhang, T. Ultrafine NiO nanosheets stabilized by TiO_2 from monolayer NiTi-LDH precursors: an active water oxidation electrocatalyst. *J. Am. Chem. Soc.* **2016**, *138*, 6517–6524.

[28] Chen, X.; Wang, Z.; Wei, Y.; Zhang, X.; Zhang, Q.; Gu, L.; Zhang, L.; Yang, N.; Yu, R. High Phase-Purity 1T-MoS_2 Ultrathin Nanosheets by a Spatially Confined Template. *Angew. Chem. Int. Ed.* **2019**, *58*, 17621–17624.

[29] Li, F.; Chen, L.; Knowles, G. P.; MacFarlane, D. R.; Zhang, J. Hierarchical mesoporous SnO_2 nanosheets on carbon cloth: a robust and flexible electrocatalyst for CO_2 reduction with high efficiency and selectivity. *Angew. Chem. Int. Ed.* **2017**, *56*, 505–509.

[30] Wang, W.; Zhu, Y. B.; Wen, Q.; Wang, Y.; Xia, J.; Li, C.; Chen, M. W.; Liu, Y.; Li, H.; Wu, H. A.; Zhai, T. Modulation of Molecular Spatial Distribution and Chemisorption with Perforated Nanosheets for Ethanol Electro-oxidation. *Adv. Mater.* **2019**, *31*, 1900528.
[31] Ren, H.; Zhao, J.; Yang, L.; Liang, Q.; Madhavi, S.; Yan, Q. Inverse opal manganese dioxide constructed by few-layered ultrathin nanosheets as high-performance cathodes for aqueous zinc-ion batteries. *Nano Res.* **2019**, *12*, 1347–1353.
[32] Dhakshinamoorthy, A.; Asiri, A. M.; Garcia, H. 2D Metal-Organic Frameworks as multifunctional materials in heterogeneous catalysis and electro/photocatalysis. *Adv. Mater.* **2019**, *31*, 1900617.
[33] Huo, Y.; Zhang, J.; Miao, M.; Jin, Y. Solvothermal synthesis of flower-like BiOBr microspheres with highly visible-light photocatalytic performances. *Appl. Catal. B-Environ.* **2012**, *111*, 334–341.
[34] Whipple, D. T.; Kenis, P. J. Prospects of CO_2 utilization via direct heterogeneous electrochemical reduction. *J. Phys. Chem. Lett.* **2010**, *1*, 3451–3458.

Manuscript received: April 9, 2020
Manuscript revised: May 13, 2020
Manuscript accepted: May 18, 2020
Accepted manuscript online: May 22, 2020

